RESEARCH ARTICLE

ADVANCED ELECTRONIC MATERIALS Open Access

www.advelectronicmat.de

# Ge Enrichment of Ge–Sb–Te Alloys as Keystone of Flexible Edge Electronics

*Sabrina Calvi,* Marco Bertelli, Sara De Simone, Francesco Maita, Simone Prili, Adriano Diaz Fattorini, Fabio De Matteis, Valentina Mussi, Flavia Righi Riva, Massimo Longo, Fabrizio Arciprete,* and Raffaella Calarco*

**Edge computing architectures are intended to store and process data nearby the sensor, while ensuring fast and safe data processing, low power consumption and cost minimization. The stability, mechanical flexibility, huge computational and storage requirements needed for these applications are beyond the capability of current embedded devices. Memories based on phase-change materials have the potential to overcome these issues. However, their behavior on flexible substrates is yet to be understood and alloys owning the required key features still need to be proposed. With this work, it is demonstrated that Ge–Sb–Te (GST) alloys are large-area scalable and directly processable on flexible substrates, while their large resistance contrast enables the prospect of multilevel data encoding. Remarkably, the Ge enrichment acts as both thermal and mechanical stabilizer within the alloy. The highlighted features of Ge-enriched GST alloys show their potential as new active materials for the most demanding flexible edge electronics applications.**

## 1. Introduction

Albeit most of the memory market is represented by high-density standalone devices, the embedded non-volatile memories are increasingly required in a wide variety of integrated circuits, with applications ranging from a few bits to megabytes for data or code storage.[1] The leading market is the automotive, followed by smartcard and microcontrollers for Internet of Things.[1,2] Lately, the demand for edge solutions was driven by the idea of moving the computing near-memory, and down to in-memory, making use of ad hoc embedded devices to safely process data physically close to the sensors. This approach lowers the power consumption, shortens the delay time, achieves real-time processing of data, has high robustness and ensures data privacy.[3] Furthermore, due to the relatively small number of bit cells, embedded memory arrays occupy a small fraction of the total die area.[1] Hence, high cell density is not essential and larger cell sizes with respect to standalone memories are still acceptable. On the other hand, the computational and storage requirements needed for edge applications are beyond the capability of current embedded devices to be implemented within a battery-limited power budget.[4] In fact, the main constraints are the low programming voltages required combined with the capability to work in harsh environments.

In this context, phase-change memories (PCRAMs) have the potential to produce reliable and low power consuming embedded electronics within the frame of edge computing.

Memories based on phase change materials (PCMs) are well known as a possible solution to overcome the von Neumann

S. Calvi, S. Prili, A. Diaz Fattorini, F. Righi Riva, F. Arciprete
Department of Physics
University of Rome Tor Vergata
Via della Ricerca Scientifica 1, Rome 00133, Italy
E-mail: sabrina.calvi@roma2.infn.it; fabrizio.arciprete@roma2.infn.it

M. Bertelli, S. De Simone, F. Maita, S. Prili, V. Mussi, M. Longo, F. Arciprete, R. Calarco
Institute for Microelectronics and Microsystems (IMM)
Consiglio Nazionale delle Ricerche (CNR)
Via del Fosso del Cavaliere 100, Rome 00133, Italy

The ORCID identification number(s) for the author(s) of this article can be found under https://doi.org/10.1002/aelm.202400184

© 2024 The Author(s). Advanced Electronic Materials published by Wiley-VCH GmbH. This is an open access article under the terms of the Creative Commons Attribution License, which permits use, distribution and reproduction in any medium, provided the original work is properly cited.

DOI: 10.1002/aelm.202400184

M. Bertelli
Institute for Microelectronics and Microsystems (IMM)
Consiglio Nazionale delle Ricerche (CNR)
Ottava strada 5, Catania 95121, Italy

F. De Matteis
Department of Industrial Engineering
University of Rome Tor Vergata
Via del Politecnico 1, Rome 00133, Italy

M. Longo
Department of Chemical Science and Technologies
University of Rome Tor Vergata
Via della Ricerca Scientifica 1, Rome 00133, Italy

architecture, by a computational memory device that can simultaneously store data and compute, carrying out calculations where the data are located.[5–8] PCMs are characterized by significantly different optical and electrical properties between their amorphous and crystalline phases.[7,9] Upon the application of a heating, these materials can be easily and reversibly switched between the phases, which are stable in ambient conditions. Their reliability was already demonstrated within rewritable optical data storage, such as DVDs and blue-ray disks, using a laser pulse as the heat source.[10] In electronic memories, the phase change is instead induced by Joule effect, producing an intrinsic nonvolatile memory with low power consumptions, fast data transfer rate and high endurance.[7,9,11] Basically, the PCRAM is a variable thin-film resistor, whose resistance at low field varies depending on the phase of the active region, which is the PCM itself.[11] If the resistivity ratio between the phases (corresponding to the SET and RESET states) is large enough, it allows for the development of multilevel memories and so enables in-memory computing.[5,6] Several architectures have been proposed for embedded PCRAMs, depending on the specific application. Considering the overwhelming compelling value required from a new technology to replace a well-assessed one, PCMs still require further investigation to combine the device performance (thermal properties, low energy consumption and speed) with its cost.[1,2,12]

In line with the circular economy model and toward the development of green electronics as well, PCM-based devices also have the potential to be fabricated with low-cost technologies on flexible and recyclable substrates.[13–15] From the embedded electronics point of view, the development of memories on flexible substrates would allow an easy integration with biosensors and harvesting devices, already well demonstrated on such substrates,[16–20] thus improving the scalability and the portability of the developed electronics. Hence, the unconventional properties of PCMs are unique for the development of edge electronics systems, considering the possibility of implementing high performance, low power consuming and stable multilevel memories directly on the flexible substrate.

However, at now phase-change materials or memories on flexible substrates have been weakly investigated.[13–15,21] As their real behavior on such substrates is still not well known, the potential of PCMs for flexible devices is far from being fully exploited. In fact, it still has to be demonstrated a phase-change alloy owning the key features required for this application, that are mainly thermal and mechanical stability while on the flexible substrate.

Within this framework and considering the stability requests from the target application field, we decided to investigate Ge-rich compositions of the family $Ge_XSb_2Te_5$ (GST X25) along the Ge-$Ge_2Sb_2Te_5$ tie-line, outside the GeTe-$Sb_2Te_3$ pseudo-binary line of the Ge–Sb–Te (GST) ternary phase diagram (**Figure 1**A). It is well assessed that these compositions can work in harsh conditions, ensuring code integrity after the chip soldering on the board and data retention in a broad temperature range.[22,23] Besides, among other chalcogenides, these alloys are already qualified for production in the embedded memory field from the top semiconductor manufacturers, such as STMicroelectronics,[23,24] making it plausible to exploit them in real applications. It is worth recalling that, during the crystallization of Ge enriched GST films, the process of Ge segregation occurs.[25–28] In the amorphous Ge-rich GST alloys, Ge atoms are expelled with successive segregation of Ge clusters, which further grow by dragging the Ge out of the matrix and crystallize above 300 °C. When the Ge concentration is low enough, crystalline GST can nucleate. Then, both the Ge and the GST crystalline phases initiate a growth process to form grains of larger sizes by coarsening and coalescence.[27] Actually, the GST crystallite composition after Ge segregation is quite independent of the initial Ge-rich composition and almost always close to the GeTe-$Sb_2Te_3$ pseudo-binary line toward the GST 124–225 compositions.[25–27] The details of the crystallization process have been debated for a long time and are strongly dependent on both composition and annealing method, leading to quite different scenarios. For example, recent works[29,30] showed that upon isothermal annealing the crystallization is divided into different phases: initially, a phase separation in the as deposited film leads to formation of Ge-rich and Ge-poor domains; then, GeTe Pnma crystals are formed triggering the heterogeneous crystallization of Ge; lastly, GST is formed from the addition of Sb in the cubic GeTe. However it proceeds, it is commonly accepted that the process of Ge segregation slows down the GST crystallization kinetics, leading to an almost linear increase in the crystallization temperature.[22,23,27] Interfaces and surface oxidation also play an important role in the crystallization of GST films. In fact, GST is a nucleation dominated materials and thus the phase transition should occur by the stochastic formation of nuclei within the GST layer (homogeneous nucleation). However, several studies highlighted that in case an oxidized surface layer is formed, crystalline nuclei are preferentially formed close to such interface via heterogenous nucleation, resulting in a lower crystallization temperature.[2] This effect becomes particularly relevant in case of Ge-rich GST since the presence of such layer favors heterogeneous crystallization of cubic Ge, which ultimately facilitate the phase separation required to initiate GST crystallization. Moreover, since in this case the crystallization preferentially proceeds from the surface toward the bulk, significant redistribution of the chemical elements occurs within the film[31,32] Nevertheless, the increase of the Ge content in the alloy results beneficial for the thermal stability of the alloy and the endurance of the PCRAM device. Practically, the Ge content in the alloy must be limited to avoid SET instabilities and too high programming currents in the memory.[23] For this motivation, we investigated the GST alloys with low-medium content of Ge. It is worth noting that memories based on Ge-rich alloys have both states affected by the drift effect, which is an undesired variation of the programmed resistance over time or temperature attributed to structural relaxation and crystallization, respectively for SET and RESET state of the residual amorphous phase at the grain boundary or of the bulk amorphous volume.[33] Nevertheless, the drift is expected to be a higher order effect and could be managed within the device by modulating the programming algorithm (e.g., tuning the write pulse in terms of shape, current level and falling time) or by properly doping the alloy with light elements to limit ion diffusion.[2,23,34]

At first, we evaluated the compatibility of these alloys with large-area scalability and their processability on flexible substrate. The behavior of these alloys on the polyimide (PI) flexible substrate was thoroughly investigated. In particular, the electronic properties and the compliance of the performance to the


© 2024 The Author(s). Advanced Electronic Materials published by Wiley-VCH GmbH

2199160x, 0, Downloaded from https://onlinelibrary.wiley.com/doi/10.1002/aelm.202400184 by CochraneItalia, Wiley Online Library on [11/09/2024]. See the Terms and Conditions (https://onlinelibrary.wiley.com/terms-and-conditions) on Wiley Online Library for rules of use; OA articles are governed by the applicable Creative Commons License

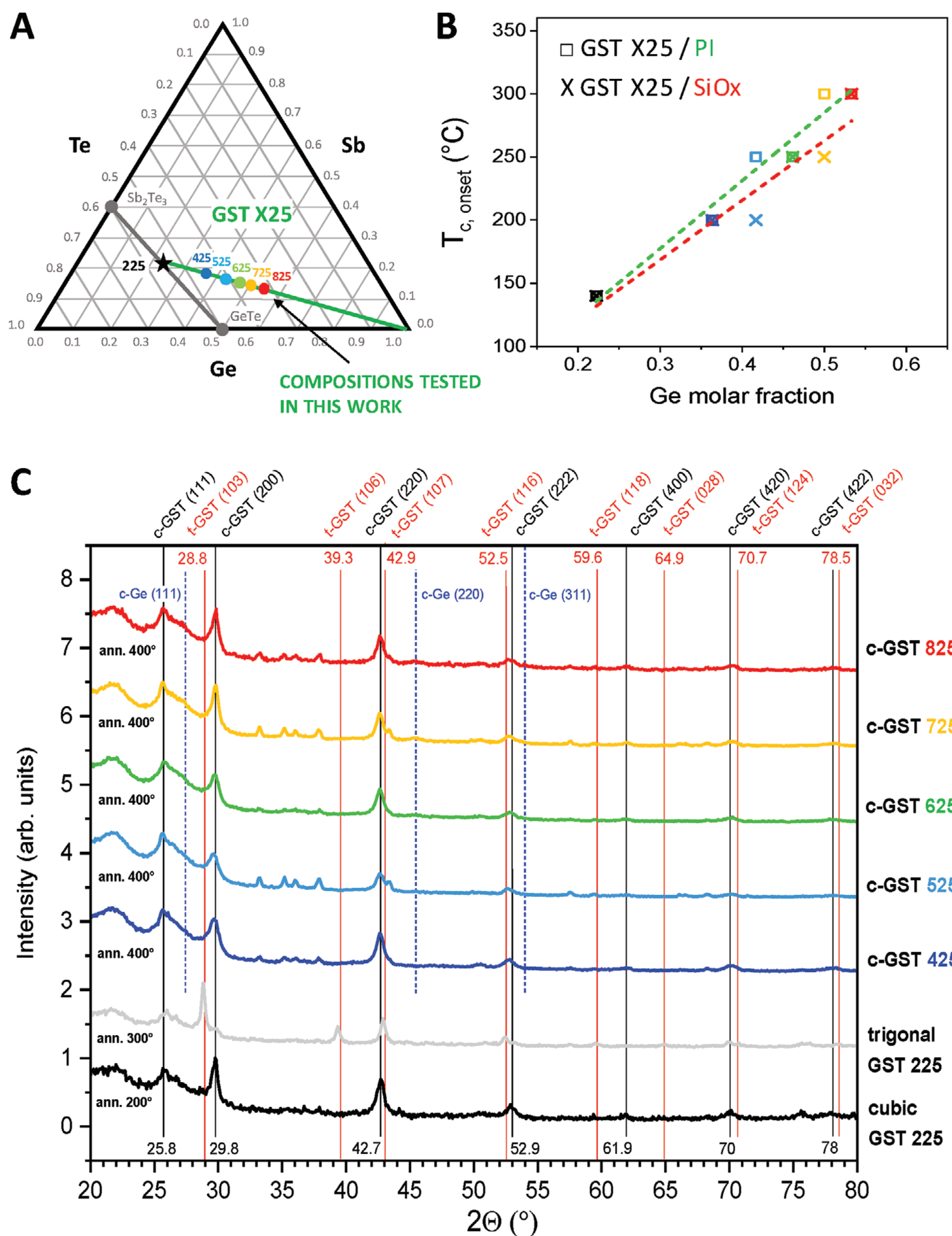


**Figure 1.** Ge-rich GST alloys on polyimide. A) Map of the GST alloys studied in this work on the GST ternary phase diagram. The compositions studied in this work are highlighted along the Ge-GST 225 green line. B) Temperature of the crystallization onset as a function of the Ge molar fraction for the Ge-rich films on PI (squares for the data fitted with the green line) and SiOx (crosses for the data fitted with the red line). C) GI-XRD data measured at RT for the cubic crystalline GST alloys deposited on PI. The trigonal GST 225 is reported too, as a reference for the reader.

target requirements were assessed with specific figures of merit, such as the resistance contrast between the amorphous and crystalline phases and the mechanical stability through bending tests. Additionally, the structural changes induced by annealing the alloys were examined to gain insights into the onset of crystallization and highlight some differences during crystallization between film deposited on PI and standard SiOx, as a reference. With this work, we unveiled the compliance of Ge enriched GST alloys to be used as active material within the most demanding flexible edge electronics applications.

## 2. Results

### 2.1. Structural Evolution Upon Annealing

As anticipated, we focused our work on the Ge-rich alloys with low-medium content of Ge. The compositions studied in this work are reported in the ternary phase diagram in Figure 1A and lie along the Ge-GST225 tie line (green line): GST 225 as a reference (black) and at increasing Ge content GST 425 (blue), GST 525 (light blue), GST 625 (green), GST 725 (yellow) and at last GST 825 (red). As for our films, it is possible to identify the


© 2024 The Author(s). Advanced Electronic Materials published by Wiley-VCH GmbH

2199160x, 0, Downloaded from https://onlinelibrary.wiley.com/doi/10.1002/aelm.202400184 by CochraneItalia, Wiley Online Library on [11/09/2024]. See the Terms and Conditions (https://onlinelibrary.wiley.com/terms-and-conditions) on Wiley Online Library for rules of use; OA articles are governed by the applicable Creative Commons License

2199160x, 0, Downloaded from https://onlinelibrary.wiley.com/doi/10.1002/aelm.202400184 by Cochraneltalia, Wiley Online Library on [11/09/2024]. See the Terms and Conditions (https://onlinelibrary.wiley.com/terms-and-conditions) on Wiley Online Library for rules of use; OA articles are governed by the applicable Creative Commons License

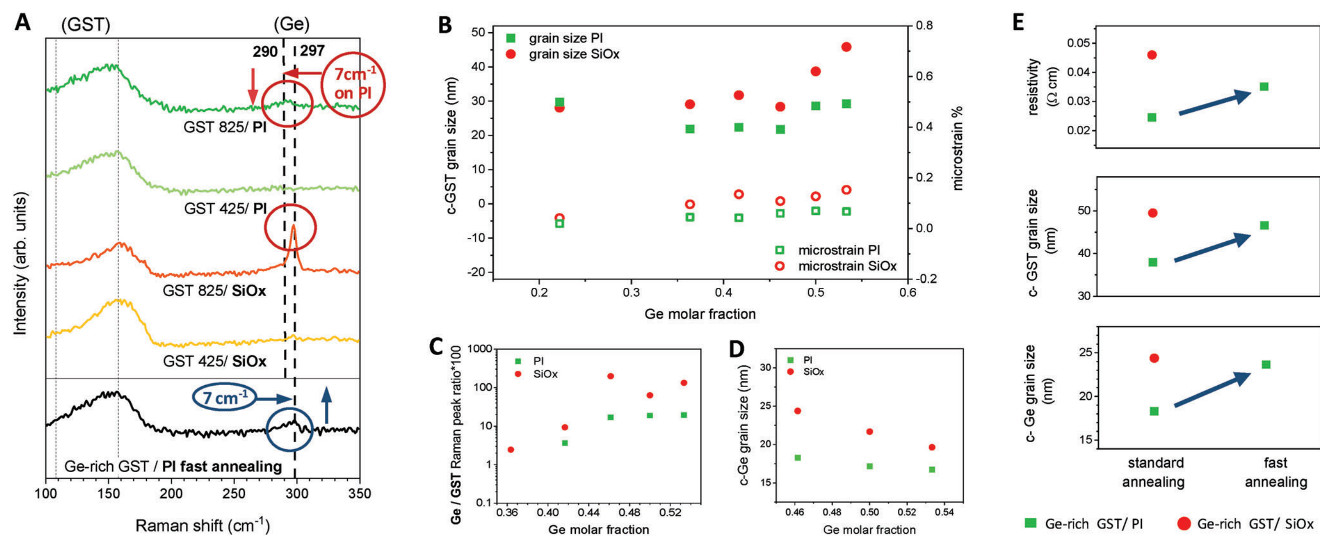

**Figure 2.** Structural evolution. A) Raman spectra of the Ge-rich GST alloys on PI and SiOx annealed with the same standard procedure, the differences are highlighted by a red circle. In the bottom panel is reported the typical spectrum for a Ge-rich film on PI after a fast annealing process. For an easier comparison, in graph A and E all the variations observed for the fast annealed Ge-rich films on PI are highlighted by the blue arrows. B) Grain size (left axis, full symbols) and microstrain (right axis, empty symbols) for cubic crystalline films, annealed with standard procedure, of Ge-rich GST on PI (green squares) and SiOx (red dots) determined from the XRD data with the WH method. C) Intensity of the c-Ge peak relative to the GST peak at 154 $cm^{-1}$ from Raman spectroscopy data as a function of the Ge molar fraction. The ratio is reported for cubic crystalline films deposited on PI substrate (green squares) and on SiOx substrate (red dots). D) Grain size of the c-Ge for films on PI (green squares) and on SiOx (red dots), annealed with standard procedure, calculated from the XRD data with the Scherrer equation. E) From top to bottom, comparison of resistivity, c-GST and c-Ge grain size, for a typical Ge-rich GST film annealed with the standard procedure on SiOx (red dots) and with the standard procedure or fast annealing on PI (green squares). For an easier comparison, in panels A and E all the variations observed for the fast annealed Ge-rich films on PI are highlighted in blue.

crystallization onset ($T_c$) observing the diffractograms as a function of the annealing temperature. The obtained $T_c$ for GST films grown on both PI and SiOx substrates are reported in Figure 1B, showing a clearly linear increasing trend at increasing Ge content. The $T_c$ calculated for films deposited on the flexible substrate (Figure 1B, squares and green line) are well in line with those from the same materials deposited in the same conditions on the rigid substrate (Figure 1B, crosses and red line). Hence, a possible interaction with the substrate leading to a different thermal conductivity in the GST film (e.g., due to a different preferred orientation[35]), is expected to be negligible compared to the Ge inclusion effect. It is worth noting that, as previously reported in the Introduction, since our films are not encapsulated it is reasonable to assume that in case a capping layer is used, $T_c$ could change by some tens of °C.

In Figure 1C are reported the Grazing Incidence X-ray Diffractograms (GI-XRD) at room temperature (RT) for GST on PI, obtained after thermal annealing as described in the Experimental Methods, where it is clearly visible the formation of the cubic crystalline phase (c-GST). The trigonal phase (t-GST) was clearly developed only in GST 225 films, as expected in this range of temperatures.[27] As detailed in the Supporting Information, the data did not show significant peak shifts for the GST films deposited on PI,[21] when compared to the corresponding films on Si wafer with thermally grown silicon oxide (SiOx), reported in Figure S2A (Supporting Information). In the case of the crystalline Ge-rich films, it is also possible to identify the Bragg reflections from crystalline Ge (c-Ge) (Figure 1C, blue lines). The c-Ge peaks do not show significant shifts for GST films on PI, when compared to both corresponding films on SiOx or pure c-Ge film (Figure 1C; *vs* Figure S2A,B, Supporting Information). Instead, the peaks are quite weaker on PI than on SiOx, although still visible for GST with Ge molar fractions higher than 0.45, while it is not possible to identify them for the GST 525 and GST 425 alloys.

In order to better appreciate the fine structural evolution of the alloys upon thermal annealing, the c-GST films were analyzed by Raman spectroscopy.[36] Particularly, in the Raman spectra the c-Ge mode appears ≈300 $cm^{-1}$ (**Figure 2A**), having increasing intensity for increasing Ge content. In Figure 2C the intensities of the c-Ge peak relative to those of the GST peak, are reported as a function of the Ge content in the alloy. It is worth noting that, comparing the c-GST films on PI and on SiOx substrates, the c-Ge peak intensity is clearly lower for the GST deposited on PI, being absent for the GST 425 alloy. Furthermore, for all the compositions the c-Ge peak position is not the same on the two substrates, showing a red shift of 7 $cm^{-1}$ for the films on PI. The lower intensity of c-Ge peaks in both diffractograms and Raman spectra, as well as the red shift of the c-Ge peak, could be reasonably explained by the formation of smaller c-Ge crystallites in the Ge-rich films grown on PI. Actually, it has been reported that gradual thermal treatments lead to the formation of small Ge nanoclusters, lowering the Ge segregation and promoting the preferential crystallization of GST;[37] besides, the dependence of the Raman peak position on the particle size has been also described for colloidal c-Ge nanocrystals,[38] in terms of a blue shift and intensity rise for increasing particle dimensions.

To clarify this aspect, the size of the c-Ge and the c-GST grains was estimated. First of all, we had to rule out that the different behavior in the GST alloy crystallization on the two substrates

 © 2024 The Author(s). Advanced Electronic Materials published by Wiley-VCH GmbH

may be caused by strain effects induced by thermal stress. A simple way to evaluate both grain size and microstrain in polycrystalline films without a preferred orientation is the Williamson–Hall (WH) plot method. The positive slope of the WH plots suggests that the crystalline Ge-rich GST films are under a small tensile strain regardless of the substrate (Figure 2B right axis). Besides, the difference in coefficients of thermal expansion (CTE) between c-GST and PI ($17.4 \times 10^{-6}$ $K^{-1}$ for c-GST 225 and $32 \times 10^{-6}$ $K^{-1}$ for PI) is lower than the one with a SiOx substrate ($0.5 \times 10^{-6}$ K).[39,40] Moreover, we highlighted that the XRD peak positions, both for c-GST (Figure 1C; Figure S2A, Supporting Information) and c-Ge (Figure S2B, Supporting Information), do not show relevant shifts for the films deposited on the two substrates. According to these results, significant strain effects due to the thermal stress can be ruled out. As for the c-GST grain size trend as a function of the Ge content (Figure 2B, left axis), it can be observed a tendency to form larger grain for alloys with high Ge contents. This could be possibly due to a reduction in the fraction of four-membered rings, which are the building blocks of the cubic crystalline phase, in favor of five and six-membered rings.[26,41] Since the basic route for the formation of cubic crystalline nuclei is the reorientation of the four-membered rings, a reduction of nuclei density might be expected by increasing the Ge content. Hence, fewer nucleation centers would allow a coarsening process of the crystalline population, resulting in the growth of enlarged grains.[27] Besides, the small pure Ge regions grow more easily at high Ge contents, by dragging the Ge excess out of the nearby GST matrix through coarsening and coalescence.[27] On the other hand, it should be pointed out that the size of the c-GST grains on PI is smaller than those on SiOx. Since the microstrain can be considered negligible for our purpose, the grain dimensions of c-Ge for the high Ge content compositions were estimated through the Scherrer equation and the obtained values confirm a smaller dimension of the c-Ge grains too, when the films are deposited on PI (Figure 2D).

As reported in Di Biagio et al.,[37] smaller nanocrystals can be induced by a gradual thermal treatment, hence delaying the crystallization kinetics. To qualitatively confirm if this hypothesis also holds true for the materials deposited on PI, Ge-rich GST films were annealed at a different rate to try to obtain a more "SiOx-like" film on PI. Compared to the standard sample, the annealing rate was increased in order for the temperature to immediately reach the final value (further details are available in the Experimental Section). This analysis is intended to give some insights into the physical phenomena behind the peculiar behavior observed on PI, without being an exhaustive study of the crystallization kinetics, which is out of the scope of this work. The Raman spectra of the fast annealed Ge-rich GST films on PI (Figure 2A bottom panel) clearly show a blue shift to the same value obtained for the films on SiOx and an increased peak intensity. Correspondingly, both the c-GST and c-Ge grain size, as well as the resistivity, increase toward the values obtained when the same GST-alloys deposited on SiOx are annealed with the standard procedure on SiOx (Figure 2E). Hence, as presumed the crystallization on PI exhibits a slower kinetics, which leads to a resistivity reduction and a smaller grain size. The main drawback reported for Ge-rich alloys during the working cycles in a PCRAM has been the increasing Ge segregation outside the device active area, which progressively pauperises the GST alloy of Ge.[23,37] Since the residual Ge-poor GST has a lower crystallization temperature the device is eventually led to failure. The different structural evolution to crystallization of Ge-rich alloys on PI might lead to lower Ge segregation, which is expected to increase the stability and endurance of the memory. Even if our work is still ongoing on this respect, it can be reasonably speculated that this behavior is due to the lower thermal conductivity of the PI with respect to the silicon (respectively, 1.8–0.12 W $mK^{-1}$ for the PI and 170–55 W $mK^{-1}$ for the Si).

### 2.2. Electronic Features

The electrical characteristics of all the studied GST alloys were measured using low electric fields, to avoid undesired phase transitions. The typical $I$–$V$ curves are reported in **Figure 3A**, for films both on PI (solid lines) and on SiOx (short dashed lines) substrates. Linear characteristics symmetrical with the voltage sign were observed for all the compositions, both for the amorphous and the cubic crystalline samples, the latter obtained after standard annealing. In Figure 3B the resistance values are plotted as a function of the probe distance for films deposited on PI and SiOx, respectively in the top and the bottom graph. These data confirm the good homogeneity of the electrical characteristics on substrate dimensions that are already of interest for the production of chips for in-memory computing. The resistivity values obtained from these data are reported in Figure 3C (dots, squares and triangles are referred to amorphous, cubic and trigonal films, respectively), showing that the resistivity increases with the Ge content in the alloy, for both phases on both substrates.

A key requirement of a PCRAM concerns the programming window, that must be large enough to avoid possible data encoding ambiguity and to reduce resistance drift effects.[7,11] Besides, the high resistance contrast enables a gradual crystallization of an amorphous region by the application of repeated pulses. Having a controllable fractional variation of the resistance extends the possible operations to the multilevel domain. In fact, it has been shown that gradual resistive switching is a basic concept for analogue computing, as it enables logic summation within a single PCRAM, as well as the implementation of neuromorphic hardware.[6] Considering our samples, the resistivity ratio between the cubic crystalline and the amorphous films is about six orders of magnitude. Particularly, the mean ratio for the Ge enriched alloys is $3.83 \times 10^6$ on PI and $2.25 \times 10^6$ on SiOx. It has to be considered that the resistance contrast of GST films is usually higher than that in memory devices. Mainly, the melt-quenched amorphized material produced by Joule effect in the memory cell has lower resistivity with respect to the amorphous as deposited phase, reducing the reset resistance. Besides, the contacts and the heater introduce parasitic resistances, increasing the set resistance of the cell.[7] Taking into account these aspects, it is worth noting that the large electrical contrast we measured is well above the minimum value for PCM films (about five orders of magnitude[7]), which is considered suitable to develop memories with an ON/OFF ratio about two orders of magnitude.[7,23,34]

To further assess the electronic features of the Ge-rich GST alloys on the flexible substrate, their optical bandgap was estimated by Visible/Near InfraRed (Vis/NIR) spectroscopy measurements.


© 2024 The Author(s). Advanced Electronic Materials published by Wiley-VCH GmbH

2199160x, 0, Downloaded from https://onlinelibrary.wiley.com/doi/10.1002/aelm.202400184 by CochraneItalia, Wiley Online Library on [11/09/2024]. See the Terms and Conditions (https://onlinelibrary.wiley.com/terms-and-conditions) on Wiley Online Library for rules of use; OA articles are governed by the applicable Creative Commons License

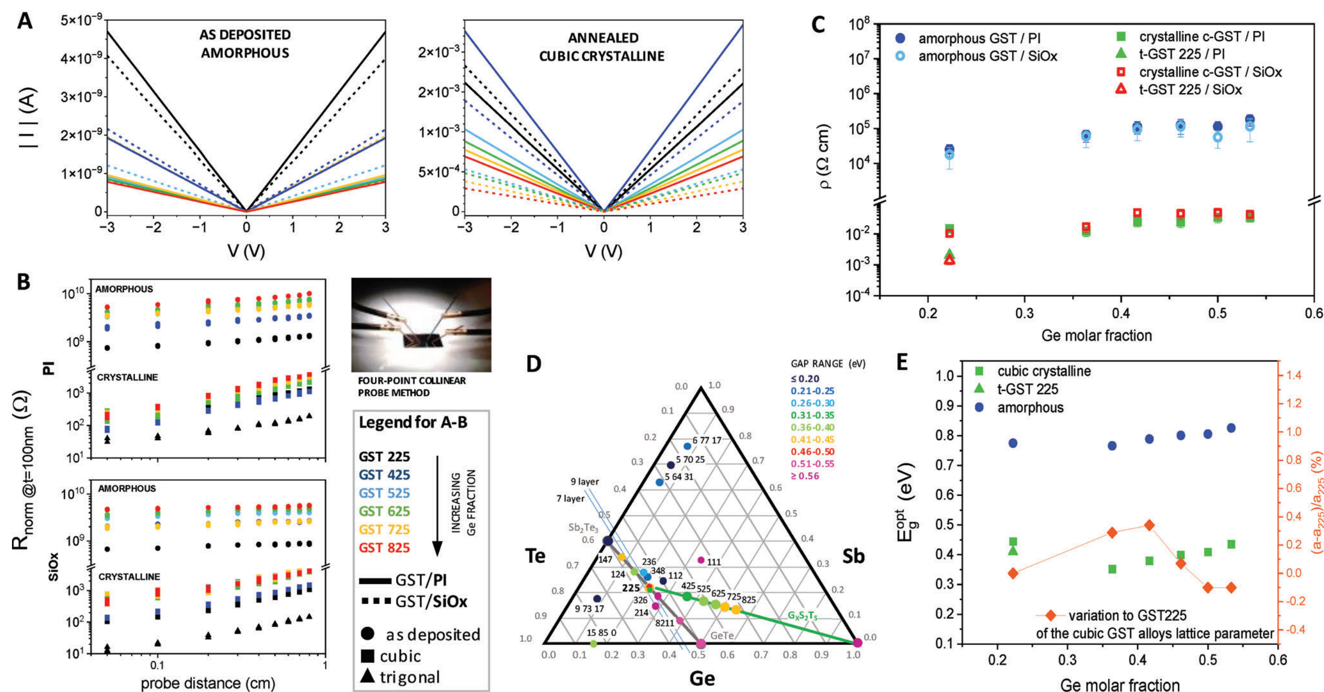


**Figure 3.** Electronic features. A) *I–V* measurements at low field for the Ge-rich GST films on PI (solid lines) and on SiOx (short dashed lines), as deposited (left graph) and after annealing to the cubic crystalline phase (right graph). B) Resistance versus probe distance for the Ge-rich GST films on PI (top graph) and on SiOx (bottom graph). A picture of the electrical measurement set-up is shown above the legend for Figure A and B. C) Resistivity of the amorphous and the crystalline Ge-rich GST films on PI and SiOx as a function of the Ge molar fraction in the alloy. D) Map of the gaps of the crystalline phase of GST alloys on the GST ternary phase diagram. Our data lie along the green line, for the other compositions the values are collected from the literature.[9,42–50] E) On the left axes (blue and green symbols), optical bandgap calculated from Vis/NIR spectroscopy data for Ge-rich GST films on PI, as deposited and crystalline, as a function of the Ge molar fraction in the alloy. On the right axes (orange symbols and line), the variation of the lattice parameter with the Ge molar fraction, calculated from the XRD data for the cubic crystalline films. The lattice parameter is reported as the relative difference in percentage with respect to those of GST 225 ($a_{225}$ = 6.0079 Å).

For the readers' reference, we reported in a GST ternary phase diagram (Figure 3D) the values obtained in this work for the crystalline films with respect to the data reported in the literature for several GST alloys.[9,42–50] It is quite clear from the map that the trend is strictly dependent not only on the composition, but also on the deviation of the alloy from the most stable phases. As for the GST X25 family of alloys under investigation, reporting the calculated values as a function of the Ge content (Figure 3E) we observe that for amorphous alloys the gap follows the resistivity trend. In the case of crystalline GST, the data highlight a difference between the GST 225 and the Ge-rich alloys. For the GST 225, the obtained gap values are well in line with those reported in the literature for films deposited on rigid substrates.[42,51,52] Just a small reduction in the gap between c-GST and t-GST can be observed, while the resistivity value differs of almost one order of magnitude. An explanation of the conduction mechanism in GST 225 is suggested by ab-initio[10] and density functional theory[53] calculations, as well as by experimental results,[54] that correlate the resistivity change between the cubic and the trigonal phase with the ordering of the vacancy distribution. On the other hand, the Ge-rich alloys have lower gaps and higher resistivities if compared to those of GST 225, with a clear trend as a function of the Ge content. It is worth recalling the crystalline structure of the c-GST 225, where Te atoms fully occupy the anionic sublattice, while Sb/Ge atoms occupy the cation sublattice with 20% of the total atomic density of vacancies, which ensure the energetic minimum introducing three p-electrons per site.[2,26,43,55] Vacancies introduce trap levels ≈100 meV above the valence band maximum, the Fermi level is then pinned close to the valence band maximum, thus causing the p-type quasi-degenerate behavior of the crystalline GST.[2,55] At low Ge enrichment, the additional Ge atoms could either be positioned at the grain boundaries or being incorporated in the GST, substitutional to Sb, interstitial or maybe occupying the vacancies even though not so energetically favored.[55] The first case seems not to occur, as the GST lattice parameter would not increase (Figure 3E, right axes). Instead, the GST lattice is expected to expand if the Ge atoms occupy interstitial sites or compensate the existing vacancies, shifting the Fermi energy toward the midgap and increasing the resistivity. Our crystalline GST 425 and GST 525 did not show such a relevant resistivity increase, while they exhibit a clear lattice expansion (Figure 3E, right axes) and gap reduction (Figure 3D,E, left axes) compared to the GST 225 values. It is worth recalling that for PCMs the gap values are strictly dependent on the annealing temperature and rate.[42,48] For example, for GST 225 in the cubic phase has been reported a gap variation from 0.5 to 0.36 eV increasing the temperature from ≈177 to 207 °C.[48] Hence, it is reasonable to observe a gap narrowing in low Ge content alloys annealed at high temperature. On the other hand, at higher Ge enrichment the Ge segregation occurs, as previously described.


© 2024 The Author(s). Advanced Electronic Materials published by Wiley-VCH GmbH

2199160x, 0, Downloaded from https://onlinelibrary.wiley.com/doi/10.1002/aelm.202400184 by Cochraneltalia, Wiley Online Library on [11/09/2024]. See the Terms and Conditions (https://onlinelibrary.wiley.com/terms-and-conditions) on Wiley Online Library for rules of use; OA articles are governed by the applicable Creative Commons License

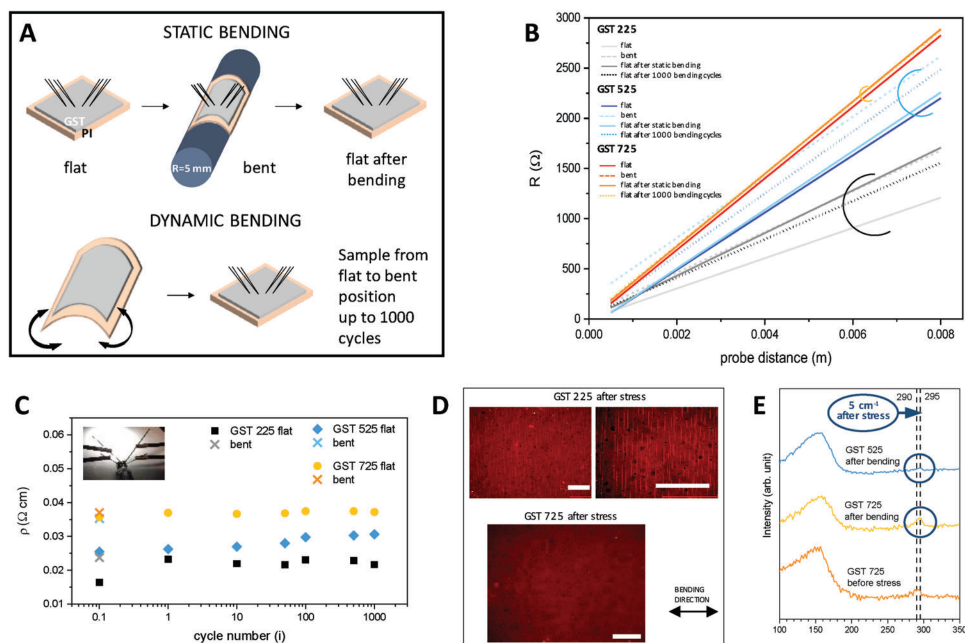


**Figure 4.** Mechanical stability. A) Scheme of the method adopted in this work for the static and dynamic bending tests. B) Linear fitting of the resistance versus probe distance data of the films during the bending tests, reported respectively for cubic crystalline GST 225 (under the black arc), GST 525 (under the light blue arc) and GST 725 (under the orange arc) on PI. Static (solid and dashed lines) bending tests and dynamic (dotted lines) bending tests after 1000 cycles. The complete data points are available in Figure S3 (Supporting Information). C) Resistivity as a function of the cycle number for the different compositions of cubic crystalline Ge-rich GST on PI. For the static bending test, a bent sample under measurement is shown in the image, while the values of resistivity of the sample flat and bent are both reported at 0.1 cycle number. D) Optical transmission microscopy images of the films after the 1000 cycles bending tests. E) Raman spectra for the Ge-rich GST on PI after the bending tests; on the bottom the spectrum of the GST 725 before any stress is reported as a reference.

In fact, above the 0.4 value of Ge molar fraction both the resistivity and the gap increase, while above the 0.45 the GST lattice parameter decreases and the GST is slightly compressed. Reasonably, at low Ge contents the Ge atoms are interstitial or partially incorporated in the GST matrix. Increasing the content of Ge, it starts being expelled leading to a crystalline Ge phase and a residual c-GST with a composition close to those along the GeTe-$Sb_2Te_3$ pseudo-binary tie-line.

### 2.3. Mechanical Behavior

The main feature of a material for flexible electronics is the ability to maintain their performance while under bending or after repeated mechanical stresses. Hence, we performed static and dynamic bending tests on the Ge-rich GST films on flexible substrates, as schematized in **Figure** 4A. For the static bending test, the resistance as a function of the probe distance was initially measured with the sample on a plane surface before any mechanical stress, then in curved position and lastly after bending in plane again. For the dynamic bending test, the sample underwent repeated bending cycles and the resistance values were collected every 10-50-100-500-1000 cycles. The tests were performed on the crystalline films, which are expected to be more sensitive to this kind of stress. Besides, compared to amorphous films, any increase in resistivity would be more easily detected and precisely quantified.

The resistance curves as a function of the probe distance of the static test and after 1000 cycles of dynamic bending are reported in Figure 4B (the complete data are available in Figure S3, Supporting Information). The static bending tests indicate that the electrical features of the GST alloys show little variation if measured under bending. The dependence of the resistance on the distance between the contacts is well described linearly in the considered range, confirming the good homogeneity of the electrical characteristics of the material on the sample area. The linear trend is confirmed during bending and after cycling. Correspondingly, the resistivity variations are negligible as can be observed from the data reported in Figure 4C. In the graph, the resistivities calculated for both tests and for the different alloys are reported as a function of the number of bending cycles.

By optical (Figure 4D) and atomic force microscopy (AFM, Figure S4, Supporting Information) observations, the films seem to be continuous, without cracks, ruptures or lacks of adhesion after the bending tests. This remark is in line with the fact that all the films still preserve the electrical continuity and good conductivity. A possible interpretation of the good mechanical behavior of these materials may lay in few peculiar features of the GST. In fact, both GST and PI are quite stiff, having rather similar high Young moduli (E = 3.2 GPa for PI and ≈30 GPa for GST 225[39,56]). Akin mechanical response is then expected under tensile stress, with little deformation. Besides, it has been already demonstrated that epilayers of van der Waals (vdW) bonded materials, such as


© 2024 The Author(s). Advanced Electronic Materials published by Wiley-VCH GmbH

2199160x, 0, Downloaded from https://onlinelibrary.wiley.com/doi/10.1002/aelm.202400184 by CochraneItalia, Wiley Online Library on [11/09/2024]. See the Terms and Conditions (https://onlinelibrary.wiley.com/terms-and-conditions) on Wiley Online Library for rules of use; OA articles are governed by the applicable Creative Commons License

GST 225, grow directly fully relaxed, therefore lattice matching with the substrate is not required.[57]

Interestingly, our bending tests highlight that the mechanical behavior of the films improves when increasing the Ge content in the alloy. At low Ge content in the alloy, we observed in the photomicrographs (Figure 4D) some straight lines not dependent on any substrate feature, but perpendicular to the bending direction and spaced down to ten microns. It is worth noting that length and number of the lines increase for decreasing Ge content in the alloy. In fact, the GST 725 after the tests do not present any morphological variation from the flat film (Figure S4, Supporting Information; Figure 4D) and its electrical characteristics are unaffected by bending stress (Figure 4B). Observing the corresponding Raman spectra of the films after the bending tests (Figure 4E), it can be noted that the c-Ge peak is clearly blue shifted. Hence, it can be deduced that the Ge crystallites are compressed after the bending stress.

To get some insights into the physical mechanism beyond these observations, it should be recalled that, in a polycrystalline material, the grain dimension affects its mechanical properties.[58,59] While in the micrometer range a grain size reduction leads to an increase in ductility, in the nanometer range a deviation from the Hall–Petch relation has been observed.[59] The nanocrystalline materials are likely to have a reduced ductility, due to a low work hardening rate, which leads to early strain localization and failure, and to a reduced capability to fix the progression of cracks by wide plastic deformation. In nanostructured materials with grain size from ≈300 nm down to 30 nm, the grain boundaries have been shown to be no longer effective for dislocation accumulation.[59,60] The grain size is so small that lattice dislocation sources are not stored inside the grain and the grain boundaries become active sources or sinks of dislocations. With finest grains, under 30 nm, the plastic deformation mechanisms are different from lattice dislocation slip. Generally, brittle behavior is expected due to the excessive volume fraction occupied by the grain boundaries, which leads to high values of the flow stress and quickly intense nanocrack generation followed by macroscopic fracture. It has been already demonstrated that the ductility might be enhanced by bimodal grain structures, with fine and coarse grains, or by second phase inclusions, respectively due to the strengthening effect provided by the large grains or the inclusions.[59,60] Considering our materials, the c-Ge nanocrystals can act as fine grain second phase inclusion, generating a strengthening effect and resulting in the increased ductility of the alloy observed.

## 3. Discussion

In this work we highlighted the unique features of Ge-rich GST as active material for flexible memories in embedded electronics.

Several remarkable features of the studied GST alloys indicate their compatibility with large-area scalability, as the possibility to process them directly on flexible substrates without a rigid carrier, as well as the good morphology and the homogeneity of their electrical characteristics on sample areas up to dimensions of interest for a chip production.

The large resistance contrast between amorphous and crystalline phases observed on the polyimide substrate is in line with the values expected from any active material to be considered suitable to develop memories with a large programming window, in order to avoid data encoding ambiguity. Properly managing the drift effects, as already demonstrated for Ge-rich alloys on rigid substrates,[34] it would allow the prospect of multilevel data encoding and so to enable operations within the multilevel domain.

Particularly, for their high crystallization onset temperature, the Ge-rich alloys ensure the stability required for the target application. If correctly exploited in a device, the observed delayed crystallization kinetics is expected to increase the stability and endurance of the memory. This interesting feature is valuable to counterbalance the performance loss typical of flexible devices.

Besides, we pointed out the excellent mechanical features of GST alloys, which are quite unique among inorganic semiconductors. After the bending tests, none of the crystalline films showed cracks, ruptures or lacks of adhesion, preserving the electrical continuity. For all the considered compositions, significant strain effects, which might have been induced by the flexible substrate, were excluded and minimal variation in the resistivity under mechanical stress was observed. Remarkably, the Ge enrichment of GST acts not only as thermal stabilizer for the alloy, but it also has a fracture toughening effect. In fact, the electrical characteristics of the GST 725 films are fully unaffected by repeated mechanical stresses.

Overall, the work done demonstrated that the Ge-rich GST features and performances are well in line with the current industrial targets for flexible edge electronics.

## 4. Experimental Section

*Alloy Deposition on the Flexible Substrate*: The GST layers were deposited by RF-sputtering in a custom-made high vacuum system (IONVAC PROCESS srl). Ge-rich GST films were deposited by co-sputtering from $Ge_2Sb_2Te_5$ and Ge targets in Ar atmosphere at RT. The GST films were deposited without adding further capping layers. The targets were provided by Robeko GmbH & Co. KG, with nominal composition within a 99.99% purity. The deposition rate was kept at 0.35–0.68 nm $s^{-1}$ depending on the composition. The thickness of the deposited layers is ≈130 nm. The GST compositions indicated throughout the paper are referred to the composition measured by X-ray fluorescence spectroscopy on the samples as deposited.

A PI foil (thickness = 75 µm) was used as the flexible substrate, due to its low thermal expansion coefficient, high thermal resistance (glass transition temperature $T_g > 300$ °C, decomposition temperature 500–600 °C) and chemical resistance. Such substrate was used free-standing without a rigid carrier, in line with the requirements for large-area compatible processes, e.g. roll-to-roll printing techniques.[61] The substrate thermal stability up to 400 °C was properly verified before growing and characterizing the PCMs. The substrate was annealed up to 400 °C and GI-XRD data were collected as a background reference for the subsequent GST film analysis (in Figure S1A, Supporting Information for the PI reference diffractogram, Figure S1B, Supporting Information for the reference diffractogram of the sample holder peaks). The thermal stability of the substrate in temperature was confirmed also by Raman and Fourier Transform Infrared measurements after annealing at 400 °C; the related data are reported in Figure S1C,D (Supporting Information).

As reference for a rigid substrate, it was used a silicon wafer 350 µm thick, with 100 nm thermally grown silicon oxide to avoid substrate-induced preferential orientations of the deposited GST layers and to allow the electrical characterization of the films. The deposition on a rigid substrate is proposed to allow a fair assessment of the GST properties on PI, having the same material deposited and characterized in the same way on the rigid and the flexible substrate. In fact, any other rigid substrate without


© 2024 The Author(s). Advanced Electronic Materials published by Wiley-VCH GmbH

2199160x, 0, Downloaded from https://onlinelibrary.wiley.com/doi/10.1002/aelm.202400184 by CochraneItalia, Wiley Online Library on [11/09/2024]. See the Terms and Conditions (https://onlinelibrary.wiley.com/terms-and-conditions) on Wiley Online Library for rules of use; OA articles are governed by the applicable Creative Commons License

a preferred orientation might have been chosen, but SiOx was preferred as it allows easy comparison with the literature.

In Figure S4 (Supporting Information) is shown a comparison of typical GI-XRD data for crystalline Ge-rich GST films on SiOx, native or thermal deposited, with or without capping layer. The data did not show significant variations, either due to the SiOx thickness and quality or to the capping layer.

*Structural Characterizations*: GI-XRD measurements were performed with a D8 Discover diffractometer (BRUKER, Cu-K$\alpha$1 radiation $\lambda = 1.5406$ Å, 40 kV and 40 mA). The DHS1100 dome-type heating stage (ANTON PAAR) was used for the characterization of the GST film structural evolution. $\omega - 2\theta$ scans ($\omega = 0.60° - 0.65°$) were acquired in the temperature range of 30 – 400 °C during sample annealing with a ramp of 60° min$^{-1}$, in $N_2$ atmosphere. The diffractograms were collected every temperature step of 50 °C. The crystallization onset ($T_c$) was defined as the temperature at which the most intense XRD peaks of the cubic phase (c-GST) appear, in particular both c-GST (200) and (220) reflections. The standard annealing was carried out with annealing rate 60 °C/min$^{-1}$, keeping the temperature constant for 25 min every 50 °C to collect the data. The fast annealing (for polyimide samples) was carried out with annealing rate 60 °C/min$^{-1}$ from RT to the final temperature, which was kept for 1 h 15 min, and the data were collected just after the annealing. The total annealing time was ≈3 h for a standard and 1 h 30 min for a fast annealing. To ensure reproducibility in the material structure, for the other measurements (electrical characterization, spectroscopy) samples annealed with the standard procedure were used; for the c-GST 225 samples annealed up to 200 °C, for the t-GST 225 samples annealed up to 300 °C, for any cubic Ge-rich GST samples annealed up to 400 °C.

Raman spectra were acquired by means of a Raman imaging microscope equipped with a 532 nm laser source, 4 mW power at the sample surface and a 50x objective (DXR2xi, THERMOFISCHER). The data acquisition was performed at RT in back-scattering geometry.

Further details on the structural characterizations are reported in the Supplementary Information (assignation of the XRD and Raman peaks; grain size determination).

*Electronic and Mechanical Characterizations*: The *I–V* characteristics in DC were measured in air in a probe station equipped with sourcemeters (KEITHLEY 2440 and 236, TEKTRONIX INC.). The four-point collinear probe technique was used to calculate the resistivity as $\rho = \pi/\ln 2 \times R \times t \times R1$, where R is the resistance, t is the film thickness and R1 the Haldor Topsøe correction factor for thin samples of finite rectangular shape.[62] The bending tests were performed with a custom-made system, equipped with a stepper motor.[63] The morphological characterization of the GST layers was performed by means of an optical microscope (CARL ZEISS AG).

The UV/Vis/NIR spectrometer used for the Tauc plot extraction was a Perkin-Elmer Lambda 19, the data were acquired in transmission mode. The absorption coefficient and the optical gap of a semiconductor ($E_g{}^{opt}$) follow the Tauc equation $\alpha h\upsilon \propto (h\upsilon - E_g^{opt})^r$, where $\alpha$ is the absorption coefficient of the material and $h\nu$ the photon energy, related to its frequency $\nu$ through the Planck's constant $h$. The optical bandgap is found from absorption spectra by linearly extrapolating to the abscissa, with $r = 2$ (indirect bandgap) for both phases.

## Supporting Information

Supporting Information is available from the Wiley Online Library or from the author.

## Acknowledgements

This work was supported by European Union's Horizon 2020 Research and Innovation program Grant Agreement No. 824957 (RC, ML, FA), Italian Ministry of University and Research program "FSE-REACT EU – PON Research and Innovation 2014–2020" (FA, SC), National Recovery and Resilience Plan (NRRP), Mission 4 Component 2 Investment 1.5 (D.M 351, 2022) (FA, ADF), National Recovery and Resilience Plan (NRRP), Mission 4 Component 2 Investment 1.5 – Call for tender No. 3277 of 30 December 2021 of the Italian Ministry of University and Research funded by the European Union – NextGenerationEU – Award Number: Project ECS 0000024 Rome Technopole (RC), and Italian Ministry of University and Research (MUR) through project PRIN2020 Emphasis CUP B87G20000160001 (RC, FA, ML, SDS), Grant MUR Dipartimento di Eccellenza 2023-27 X-CHEM project "eXpanding CHEMistry: implementing excellence in research and teaching" (ML).

## Conflict of Interest

The authors declare no conflict of interest.

## Author Contributions

S.C., F.A., M.L., and R.C. performed conceptualization; S.C., S.P., and F.M. performed methodology; M.B., S.D.S., F.M., F.D.M., V.M., and S.C. acquired resources; M.B., S.D.S., S.P., S.C., A.D.F., and F.R.R. performed investigation; S.C., M.B., and S.D.S. performed formal analysis; S.C. performed data curation; S.C. and M.B. performed validation; S.C. performed visualization; S.C. wrote the original draft; S.C., F.A., M.L., R.C., F.M., S.P., and V.M. reviewed and edited the final manuscript; F.A., M.L., and R.C. performed project administration; F.A., M.L., and R.C. performed funding acquisition.

## Data Availability Statement

The data that support the findings of this study are available from the corresponding author upon reasonable request.

## Keywords

edge electronics, flexible electronics, Ge-rich alloys, Ge–Sb–Te (GST), phase-change materials (PCM)

Received: March 28, 2024
Revised: June 12, 2024
Published online:

[1] G. Molas, E. Nowak, *Appl. Sci.* **2021**, *11*, 11254.
[2] (Ed.: A. Redaelli), *Phase Change Memory*, Springer International Publishing, Cham, **2018**.
[3] L. Greco, G. Percannella, P. Ritrovato, F. Tortorella, M. Vento, *Pattern Recognit. Lett.* **2020**, *135*, 346.
[4] I. Ben Dhaou, M. Ebrahimi, M. Ben Ammar, G. Bouattour, O. Kanoun, *Electronics* **2021**, *10*, 2104.
[5] D. Ielmini, S. Ambrogio, *Nanotechnology* **2020**, *31*, 092001.
[6] D. Ielmini, H.-S. P. Wong, *Nat. Electron.* **2018**, *1*, 333.
[7] H.-S. P. Wong, S. Raoux, S. Kim, J. Liang, J. P. Reifenberg, B. Rajendran, M. Asheghi, K. E. Goodson, *Proc. IEEE* **2010**, *98*, 2201.
[8] P. Hosseini, A. Sebastian, N. Papandreou, C. D. Wright, H. Bhaskaran, *IEEE Electron Device Lett.* **2015**, *36*, 975.
[9] K. Shportko, S. Kremers, M. Woda, D. Lencer, J. Robertson, M. Wuttig, *Nat. Mater.* **2008**, *7*, 653.
[10] M. Wuttig, N. Yamada, *Nat. Mater.* **2007**, *6*, 824.
[11] (Eds.: M. Rudan, R. Brunetti, S. Reggiani), *Springer Handbook of Semiconductor Devices*, Springer International Publishing, Cham, **2023**.
[12] K. Prall, in *2017 IEEE Int. Mem. Workshop IMW*, *6*, 1 (IEEE, **2017**).


© 2024 The Author(s). Advanced Electronic Materials published by Wiley-VCH GmbH

2199160x, 0, Downloaded from https://onlinelibrary.wiley.com/doi/10.1002/aelm.202400184 by CochraneItalia, Wiley Online Library on [11/09/2024]. See the Terms and Conditions (https://onlinelibrary.wiley.com/terms-and-conditions) on Wiley Online Library for rules of use; OA articles are governed by the applicable Creative Commons License

[13] S.-H. Hong, J.-H. Jeong, K.-I. Kim, H. Lee, *Microelectron. Eng.* **2011**, *88*, 2013.
[14] B. H. Mun, B. K. You, S. R. Yang, H. G. Yoo, J. M. Kim, W. I. Park, Y. Yin, M. Byun, Y. S. Jung, K. J. Lee, *ACS Nano* **2015**, *9*, 4120.
[15] A. I. Khan, A. Daus, R. Islam, K. M. Neilson, H. R. Lee, H.-S. P. Wong, E. Pop, *Science* **2021**, *373*, 1243.
[16] S. Calvi, M. Rapisarda, A. Valletta, M. Scagliotti, S. De Rosa, L. Tortora, P. Branchini, L. Mariucci, *Org. Electron.* **2022**, *102*, 106452.
[17] S. Calvi, L. Basiricò, S. M. Carturan, I. Fratelli, A. Valletta, A. Aloisio, S. De Rosa, F. Pino, M. Campajola, A. Ciavatti, L. Tortora, M. Rapisarda, S. Moretto, M. Verdi, S. Bertoldo, O. Cesarini, P. Di Meo, M. Chiari, F. Tommasino, E. Sarnelli, L. Mariucci, P. Branchini, A. Quaranta, B. Fraboni, *Npj Flex. Electron.* **2023**, *7*, 5.
[18] F. Pino, J. C. Delgado, S. M. Carturan, G. Mantovani, M. Polo, D. Fabris, G. Maggioni, A. Quaranta, S. Moretto, *Sci. Rep.* **2023**, *13*, 4799.
[19] L. Maiolo, F. Maita, A. Castiello, A. Minotti, A. Pecora, in *2017 IEEE Int. Workshop Metrol. Aerosp. MetroAeroSpace*, IEEE, Piscataway, NJ **2017**, pp. 271.
[20] M. Rapisarda, S. Calvi, A. Valletta, G. Fortunato, L. Mariucci, M. Greco, V. Vinciguerra, in *Nanotechnol. IEEE-NANO 2015 IEEE 15th Int. Conf. On*, IEEE, Hoboken NJ **2015**, pp. 1430.
[21] M. Bertelli, A. Díaz Fattorini, S. De Simone, S. Calvi, R. Plebani, V. Mussi, F. Arciprete, R. Calarco, M. Longo, *Nanomaterials* **2022**, *12*, 2001.
[22] P. Zuliani, E. Varesi, E. Palumbo, M. Borghi, I. Tortorelli, D. Erbetta, G. D. Libera, N. Pessina, A. Gandolfo, C. Prelini, L. Ravazzi, R. Annunziata, *IEEE Trans. Electron Devices* **2013**, *60*, 4020.
[23] A. Redaelli, E. Petroni, R. Annunziata, *Mater. Sci. Semicond. Process.* **2022**, *137*, 106184.
[24] M. Baldo, L. Laurin, E. Petroni, G. Samanni, M. Allegra, E. Gomiero, D. Ielmini, A. Redaelli, in *2022 IEEE Int. Mem. Workshop IMW*, IEEE, Dresden, Germany, **2022**, pp. 1–4.
[25] L. Prazakova, E. Nolot, E. Martinez, D. Rouchon, F. Fillot, N. Bernier, R. Elizalde, M. Bernard, G. Navarro, *Materialia* **2022**, *21*, 101345.
[26] O. Abou El Kheir, M. Bernasconi, *Nanomaterials* **2021**, *11*, 2382.
[27] M. A. Luong, M. Agati, N. Ratel Ramond, J. Grisolia, Y. Le Friec, D. Benoit, A. Claverie, *Phys. Status Solidi RRL – Rapid Res. Lett.* **2021**, *15*, 2000471.
[28] D. Baratella, O. A. E. Kheir, M. Bernasconi, arXiv preprint arXiv:2004.15128, **2024**.
[29] E. Rahier, S. Ran, N. Ratel Ramond, S. Ma, L. Calmels, S. Saha, C. Mocuta, D. Benoit, Y. Le Friec, M. A. Luong, A. Claverie, *ACS Appl. Electron. Mater.* **2022**, *4*, 2682.
[30] E. Rahier, M.-A. Luong, S. Ran, N. Ratel-Ramond, S. Saha, C. Mocuta, D. Benoit, Y. Le-Friec, A. Claverie, *Phys. Status Solidi RRL – Rapid Res. Lett.* **2023**, *17*, 2200450.
[31] M. Agati, C. Gay, D. Benoit, A. Claverie, *Appl. Surf. Sci.* **2020**, *518*, 146227.
[32] L. Goffart, B. Pelissier, G. Lefèvre, Y. Le–Friec, C. Vallée, G. Navarro, J. Reynard, *Appl. Surf. Sci.* **2022**, *573*, 151514.
[33] N. Ciocchini, E. Palumbo, M. Borghi, P. Zuliani, R. Annunziata, D. Ielmini, *IEEE Trans. Electron Devices* **2014**, *61*, 2136.
[34] F. Arnaud, P. Zuliani, J. P. Reynard, A. Gandolfo, F. Disegni, P. Mattavelli, E. Gomiero, G. Samanni, C. Jahan, R. Berthelon, O. Weber, E. Richard, V. Barral, A. Villaret, S. Kohler, J. C. Grenier, R. Ranica, C. Gallon, A. Souhaite, D. Ristoiu, L. Favennec, V. Caubet, S. Delmedico, N. Cherault, R. Beneyton, S. Chouteau, P. O. Sassoulas, A. Vernhet, Y. Le Friec, F. Domengie, et al., in *2018 IEEE Int. Electron Devices Meet. IEDM* **2018**, IEEE, San Francisco, CA, p. 18.4.1-18.4.4.
[35] T.-R. Wei, P. Hu, H. Chen, K. Zhao, P. Qiu, X. Shi, L. Chen, *Appl. Phys. Lett.* **2019**, *114*, 053903.
[36] P. M. Fauchet, I. H. Campbell, *Crit. Rev. Solid State Mater. Sci.* **1988**, *14*, s79.
[37] F. Di Biagio, S. Cecchi, F. Arciprete, R. Calarco, *Phys. Status Solidi RRL – Rapid Res. Lett.* **2019**, *13*, 1800632.
[38] C. E. Bottani, C. Mantini, P. Milani, M. Manfredini, A. Stella, P. Tognini, P. Cheyssac, R. Kofman, *Appl. Phys. Lett.* **1996**, *69*, 2409.
[39] I.-M. Park, J.-K. Jung, S.-O. Ryu, K.-J. Choi, B.-G. Yu, Y.-B. Park, S. M. Han, Y.-C. Joo, *Thin Solid Films* **2008**, *517*, 848.
[40] T. Imajo, T. Suemasu, K. Toko, *Sci. Rep.* **2021**, *11*, 8333.
[41] J. Hegedüs, S. R. Elliott, *Nat. Mater.* **2008**, *7*, 399.
[42] B.-S. Lee, J. R. Abelson, S. G. Bishop, D.-H. Kang, B. Cheong, K.-B. Kim, *J. Appl. Phys.* **2005**, *97*, 093509.
[43] Y. Saito, A. V. Kolobov, P. Fons, K. V. Mitrofanov, K. Makino, J. Tominaga, J. Robertson, *Appl. Phys. Lett.* **2019**, *114*, 132102.
[44] A.-K. U. Michel, M. Wuttig, T. Taubner, *Adv. Opt. Mater.* **2017**, *5*, 1700261.
[45] Z. Wu, S. Lee, Y.-W. Park, H.-W. Ahn, D. S. Jeong, J. Jeong, K. No, B. Cheong, *Appl. Phys. Lett.* **2010**, *96*, 133510.
[46] T. D. Kang, A. Sirenko, J.-W. Park, H. S. Lee, S. Lee, J. Jeong, B. Cheong, H. Lee, *J. Electrochem. Soc.* **2011**, *158*, H249.
[47] J. Kaur, A. Parmar, S. K. Tripathi, N. Goyal, *Mater. Res. Express* **2019**, *6*, 046417.
[48] S. Sahu, A. Manivannan, U. P. Deshpande, *J. Phys. Appl. Phys.* **2018**, *51*, 375104.
[49] T. Kato, K. Tanaka, *Jpn. J. Appl. Phys.* **2005**, *44*, 7340.
[50] J.-W. Park, S. H. Eom, H. Lee, J. L. F. Da Silva, Y.-S. Kang, T.-Y. Lee, Y. H. Khang, *Phys. Rev. B* **2009**, *80*, 115209.
[51] A. Pirovano, A. L. Lacaita, A. Benvenuti, F. Pellizzer, R. Bez, *IEEE Trans. Electron Devices* **2004**, *51*, 452.
[52] Z. Xu, C. Chen, Z. Wang, K. Wu, H. Chong, H. Ye, *RSC Adv.* **2018**, *8*, 21040.
[53] W. Zhang, A. Thiess, P. Zalden, R. Zeller, P. H. Dederichs, J.-Y. Raty, M. Wuttig, S. Blügel, R. Mazzarello, *Nat. Mater.* **2012**, *11*, 952.
[54] V. Bragaglia, F. Arciprete, W. Zhang, A. M. Mio, E. Zallo, K. Perumal, A. Giussani, S. Cecchi, J. E. Boschker, H. Riechert, S. Privitera, E. Rimini, R. Mazzarello, R. Calarco, *Sci. Rep.* **2016**, *6*, 23843.
[55] D. Lencer, M. Salinga, M. Wuttig, *Adv. Mater.* **2011**, *23*, 2030.
[56] Y. Won, J. Lee, M. Asheghi, T. W. Kenny, K. E. Goodson, *Appl. Phys. Lett.* **2012**, *100*, 161905.
[57] E. Zallo, S. Cecchi, J. E. Boschker, A. M. Mio, F. Arciprete, S. Privitera, R. Calarco, *Sci. Rep.* **2017**, *7*, 1466.
[58] "Materials Science and Engineering: An Introduction, 10th ed. | Wiley," https://www.wiley.com/en-us/Materials+Science+and+Engineering%3A+An+Introduction%2C+10th+Edition-p-9781119405498.
[59] M. A. Meyers, A. Mishra, D. J. Benson, *Prog. Mater. Sci.* **2006**, *51*, 427.
[60] I. A. Ovid'ko, *Rev. Adv. Mater. Sci.* **2005**, *10*, 89.
[61] S. Calvi, F. Maita, M. Rapisarda, G. Fortunato, A. Valletta, V. Preziosi, A. Cassinese, L. Mariucci, *Org. Electron.* **2018**, *61*, 104.
[62] D. K. Schroder, *Semiconductor Material and Device Characterization*, John Wiley & Sons, Inc., Publication, Hoboken, NJ **2006**.
[63] E. Palmieri, L. Maiolo, I. Lucarini, A. D. Fattorini, E. Tamburri, S. Orlanducci, R. Calarco, F. Maita, *Adv. Mater. Technol.* **2024**, *9*, 2301282.


© 2024 The Author(s). Advanced Electronic Materials published by Wiley-VCH GmbH

2199160x, 0, Downloaded from https://onlinelibrary.wiley.com/doi/10.1002/aelm.202400184 by CochraneItalia, Wiley Online Library on [11/09/2024]. See the Terms and Conditions (https://onlinelibrary.wiley.com/terms-and-conditions) on Wiley Online Library for rules of use; OA articles are governed by the applicable Creative Commons License